Design and analysis of a Circulatory Assistance Benchmark Actuator for an Artificial Lung

A. Sahnoune, Maya Hage-Hassan, Guillaume Krebs, Claude Marchand, Julien Guihaire, Olaf Mercier

Design and analysis of a Circulatory Assistance Benchmark Actuator for an Artificial Lung

A. Sahnoune, M. Hage-Hassan, G. Krebs, C. Marchand, J. Guihaire, O. Mercier

2022 International Conference on Electrical Machines (ICEM) | 978-1-6654-1432-6/22/$31.00 ©2022 IEEE | DOI: 10.1109/ICEM51905.2022.9910858

***Abstract* – The ANR RHU Bio Art-Lung 2020 project aims to develop an extracorporeal artificial lung with reduced size and mass. An essential element of the system is its circulatory assist centrifugal pump, which ensures blood circulation. This article outlines the electrical motor's specifications and then presents an initial dimensioning using a design of experiments method. The final structure obtained from the sensitivity study is analyzed using 2D and 3D finite element (FE) methods. The motor performances resulting are compared to experimental results. Good concordance is shown between the test and finite element analysis (FEA).**

***Index Terms*--Circulatory assistance pumps, electric actuators, design of experiments, finite element modelling.**

I. Introduction

Many patients with heart or respiratory failure are not eligible for a cardiopulmonary transplant because they are too old or weak. Artificial organs represent an alternative to compensate these organ deficiencies, which are sometimes refractory to medical treatment. To date, there is no artificial lung to support respiratory function for several weeks while waiting for a transplant. The artificial lung developed in the ANR RHU BioArt Lung 2020 project should help patients with chronic respiratory failure.

In this project, a brand XENIOS DP3 pump, see Fig. 1, is used with an extracorporeal oxygenation membrane (ECMO). This pump consists of a disposable head fitted with a turbine and an electric motor magnetically coupled to the turbine via a shaft and a two magnetic disk. The turbine has a magnetic ring Fig. 2 with four poles. The rotation of the motor drives the first disc, and the latter sets the turbine in motion.

This fully functional device has several drawbacks: its weight (1.67 kg), the acoustic noise generated during operation and low efficiency. The objective of the presented works is to design a compact electric motor with the same specifications of the initial actuator.

A permanent magnet synchronous motor (PMSM) is proposed for this application. In this paper, its optimal design is described as well as a validation on an experimental bench. First, PMSM design specifications and optimal design are described in detail. Second, the performances of the actuator are analysed using FEMM and COMSOL for 2D and 3D finite element analyses (FEA). To finish, the prototype and experimental bench are presented and a comparison with numerical results is proposed.

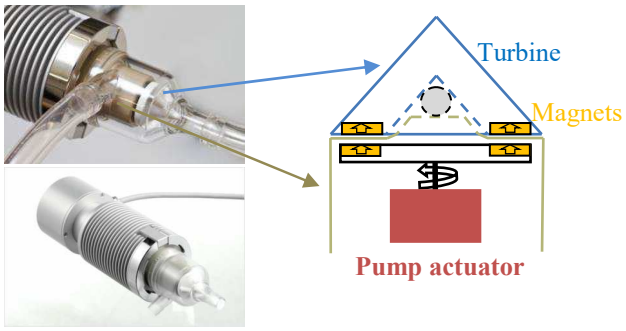

Fig. 1. XENIOS DP3 pump (left), sectional drawing of the pump (right).

Fig. 2. XENIOS DP3 pump head (left), pump impeller (center and right).

II. Machine Type and Design Considerations

A. Actuator Specifications

As part of establishing of extracorporeal blood circulation to a portable artificial lung, a flow rate of 2.5 L/min must be ensured over a wide range of pressure drops (length of the cannulas, oxygenator of the artificial lung) between 0 and 300 mmHg.

The pump head described in Fig. 2 is a device under medical standards; its outer diameter is constrained to 25 mm. In order not to denature the blood, the critical temperature of the pump should not exceed 42°C [1]. The battery that will power the device delivers a maximum current of 10 A for a voltage of 12 V. The speed range varies between 2000 and 10 000 rpm to limit risks of hemolysis and thrombosis. Table I summarizes the specifications.

TABLE I
Initial Motor Design Data

Parameters	Specifications (Units)
Speed range	$[2000 - 10\,000](rpm)$
Maximum voltage	$12\ (V)$
Maximum current	$10\ (A)$
Nominal torque	$> 20\ (mNm)$
External diameter	$25\ (mm)$
Total length	$30\ (mm)$
Current density	$7\ (A/mm^2)$
Slot filling factors	0.55
External temperature	$42\ (°C)$

This work is part of the BioArt-Lung project coordinated by Marie Lannelongue Hospital and financed by the French National Agency for Research (ANR).

A. Sahnoune, M. Hage-Hassane, G. Krebs, C. Marchand, are with Paris-Saclay University, CentraleSupélec, CNRS, Laboratory of Electrical and Electronic Engineering of Paris, 91192, Gif-sur-Yvette, France
Contact mail: (e-mail: guillaume.Krebs@centralesupelec.fr).

A. Sahnoune, J. Guihaire, O. Mercier. are with Marie Lannelongue Hospital, Research and Innovation Unit, 133 Avenue de la Résistance, 92350, Le Plessis-Robinson, France.
Contact mail: (e-mail: O.MERCIER@ghpsj.fr).

B. Motor Type

Fig. 3 shows the chosen permanent magnet synchronous motor (PMSM) type. The simplicity of this machine makes it possible to obtain a reference machine quickly. The 3 phases motor is also prototyped to highlight technical difficulties. The motor consists of twelve teeth with concentred winding and four pole pairs of neodymium-iron-boron (NdFeB) magnets mounted on the surface of the rotor. Furthermore, the winding location permits avoiding short-circuits between two phases

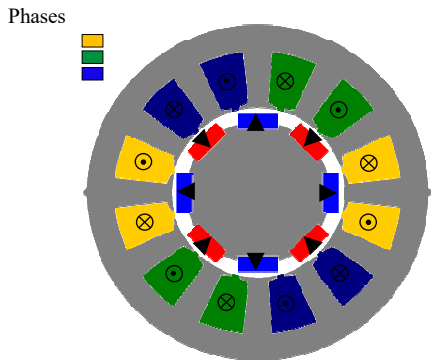

Fig. 3. Geometry of the chosen reference PMSM.

To study several structures, a method based on the design of experiments [2-4] was chosen. It makes it possible to analyse the effect of the chosen geometric variables on the chosen efficiency: torque, weight, efficiency, as well as the level of voltage.

C. Structure Design

The design of the PMSM is carried out using the experimental design method coupled with a 2D finite element analysis. When the motor dimensions are modified, a new finite element mesh is automatically generated. This method allowed us to validate the influential geometric variables in order to achieve the first geometry. The modeling is validated by an optimization resolved using the fmincon function in MATLAB with sequential quadratic programming (SQP). We choose four parameters as design variables, which define the whole shape of the stator and rotor assuming a constant motor volume and a constant air-gap length. The external diameter of the machine and the length of the machine are set at 25 mm and 30 mm respectively and 0.4 mm for the air-gap, as shown in Fig. 4.

Full factorial design of experiments is used on the totality of the domain, and it implicitly imposes the number of experiments to be done. It depends on the number of factors and on the number of levels for each of them. For n factors, m level designs are fully defined with [2-4]:

$$N_{experiments} = n^m \tag{1}$$

The domain of variation of a factor is limited between a lower limit and an upper limit.

The four parameters chosen are, the radius of the stator yoke (R_{yoke}), the radius of the stator teeth (R_{teeth}), the radius of the magnets (R_{mag}) and finally the slot-opening angle (δ). The coefficients ($\alpha_{Yoke}, \alpha_{teeth}, \alpha_{Magnet}, \alpha_{slot\_pening}$) allowing the calculation of the parameters are defined as follows:

$$\begin{aligned} R_{Yoke} &= \alpha_{Yoke}\, R_{Ext} \\ R_{Teeth} &= \alpha_{teeth}\, R_{Yoke} \\ R_{magnet} &= \alpha_{Magnet}\, R_{Teeth} \end{aligned} \tag{2}$$

With $R_{ext} = 12.5\ mm$

The coefficient allowing the calculation of the slot-opening angle δ of the stator teeth is noted $\alpha_{slot\_opening}$ and corresponds to the fourth variable:

$$\delta = \alpha_{Slot_{opening}} \frac{2\pi}{N_e} \tag{3}$$

With $N_e = 12$ the number of slots.

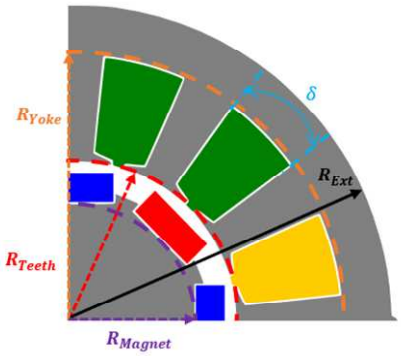

Fig. 4. Variables used in the design of experiments.

The design domain in Eq. 4 is chosen to guarantee the feasibility of the machine while respecting the specifications. They are as follows:

$$\begin{aligned} \alpha_{Yoke} &\in [0.60\,, 0.85] \\ \alpha_{Teeth} &\in [0.40\,, 0.70] \\ \alpha_{Magnet} &\in [0.30\,, 0.90] \\ \alpha_{Slot_{opening}} &\in [0.40\,, 0.60] \end{aligned} \tag{4}$$

To reduce the computation time, the average torque under load is determined by the mean value over four positions [5] as presented below:

$$\langle C \rangle = \frac{1}{4}\left(C_0 + C_{\pi/12} + C_{\pi/6} + + C_{\pi/4}\right) \tag{5}$$

Where C_i is the torque computation, with $\left\{0, \frac{\pi}{12}, \frac{\pi}{6}, \frac{\pi}{4}\right\}$ for the position.

The voltage is defined by equation:

$$v(t) = R_{ph} i(t) + \frac{d\Phi}{dt} \tag{6}$$

Φ, R_{ph}, i correspond to the total magnetic flux, resistance of one phase and current respectively.

After a few iterations, a compromise must be done to maximize the torque and limit the induced voltage while respecting the specifications. The parametric coefficients values which converge to the optimum torque are: (0.84, 0.6, 0.49, 0.4). Fig. 5 shows the variation of the average torque of different structures as a function of the chosen geometric

variables. The figure shows that the torque variation is between 22 and 73 mNm.

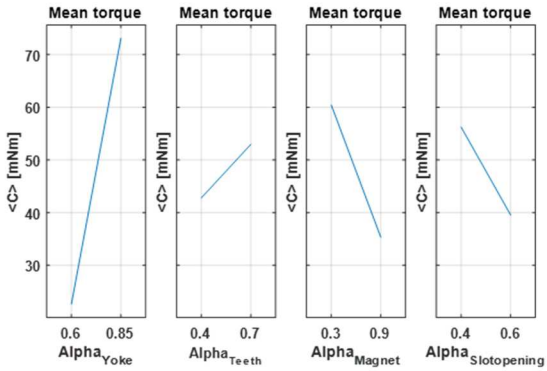

Fig. 5. The average torque for different designs obtained from DOE with 625 runs vs. the parametric coefficients.

The dimensions of the structure obtained with the optimum values are given in Table II.

TABLE II
DESIGN PARAMETER OF THE OPTIMAL PMSM

Characteristics: Symbols	Values (Units)
Machine outer radius : R_{out}	12.5 (mm)
Stator yoke thickness: e_{yoke}	1.5 (mm)
Stator tooth height: H_{st}	4.2 (mm)
thickness of magnets: e_{mag}	1.2 (mm)
Air gap: e	0.4 (mm)
Stack length: l_s	30 (mm)
Number of Turns: N_s	29
Active part mass: m	72 (g)

To verify the desired electromagnetic performance, a serie of finite element validations were implemented.

III. PERFORMANCE ANALYSIS

A. Magnetic Analysis

The PMSM is modelled by 2D and 3D Finite Element (FE) methods in FEMM and Comsol®; to validate the proposed design and lead to the prototype. Both no-load and load analyses are performed. The no-load flux density distribution of the machine is illustrated in Fig. 6. It shows that flux density levels are acceptable for this motor and maximum level is obtained at stator teeth as almost 1.6 T.

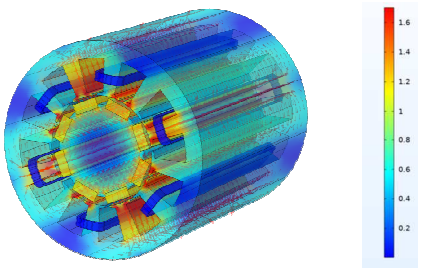

Fig. 6. No-load flux density distribution inside the motor.

One of the most critical components of PM motors is cogging torque, especially for direct-drive PMSM, since it causes unwanted harmonics and distortion on the output torque and noise [6]. In addition, if the application requires precise control at low speeds, it must be eliminated. Cogging torque variations displayed in Fig.7 are modelled using both 2D and 3D FEA.

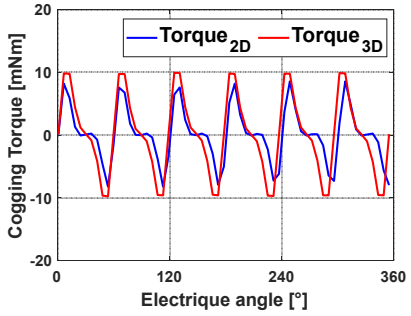

Fig. 7. Cogging torque variation obtained from FEA.

The amplitude of the torque ripples is about 30% of the of the machine's average measured. It should be noted that the maximum cogging value is about 40% of the nominal torque (20 mNm), which is a relatively large value. Further investigation is necessary to verify if it will not cause a vibratory problem to the pump. It is essential to consider this aspect for such small PM motors. The no-load flux results and the phase back-EMF voltage waveforms at 5000 rpm obtained by EF 2D and 3D are illustrated in Fig. 8 and 9. The relative difference between these two models is 3%, which gives confidence to this modelling.

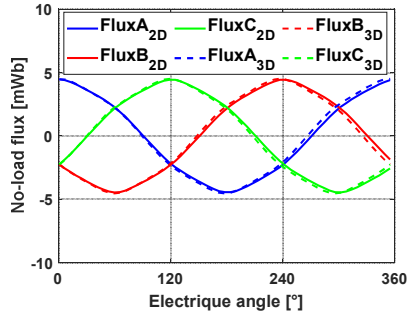

Fig. 8. No-load flux waveforms between 2D and 3D FE.

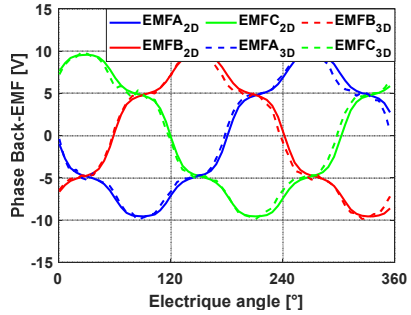

Fig. 9. Phase back-EMF waveform comparison between 2D and 3D FE at 5000 rpm rotor speed.

Fig. 10 display the back-EMF harmonic content at 5000 rpm rotor speed. The back-EMF variation shows that the harmonic content is relatively low, and the motor has a

slightly high total harmonic distortion (8%). It can be said that the back-EMF waveform has very low harmonic content.

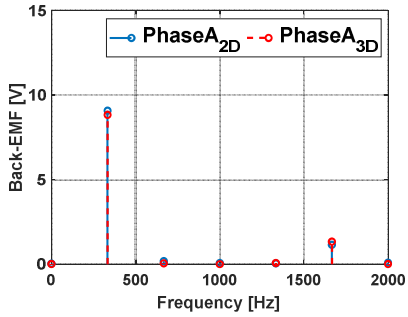

Fig. 10. Back-EMF harmonics obtained from FEA at 5000 rpm rotor speed.

On-load FE analysis of the motor is performed, and the torque output waveforms obtained by 2D and 3D FEA at 1.5 Arms are compared. The results are given in Fig. 11. The average torque values and torque ripple obtained from both 2D and 3D FEA (calculated using Maxwell's tensor) are extremely close to each other. The machine can deliver torque under load with an average value of 56.9 mNm. The value of the torque obtained is greater than the nominal torque of the machine. This difference ensures a comfortable margin of work.

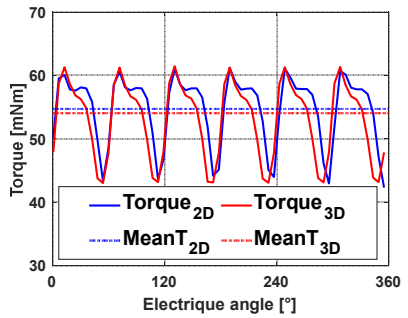

Fig. 11. Torque output comparison between 2D and 3D FEA (@1.5 Arms).

The iron loss calculation model used [7] is given in equation (10). This model includes hysteresis losses, eddy current losses (known as classic), and additional losses:

$$P_h = \alpha f B_p^x \quad (7)$$

$$P_e = e f^{1,5} B_p^{1,5} \quad (8)$$

$$P_{ec} = b f^2 B_p^2 \quad (9)$$

$$P_{Iron\ Loss} = \sum P_h + P_e + P_{ec} \quad (10)$$

With B_p is the peak value of the magnetic induction. f is the frequency of magnetic induction. The coefficients α, b, e, x: are identified using data provided by the manufacturers. The maximum efficiency of the PMSM has been estimated to be 85 %. The weight of the active parts of the machine is approximately 100 g.

B. Thermal Analysis

Many thermal models have given satisfactory results for evaluating permanent magnet motor heating. This study chose a simplified model based on [8-10]. In this section, a simplified thermal model is presented. It allows to quickly calculate the different temperatures at the level of the machine in a steady state. We are particularly interested in the temperature rise at the outer periphery of the device to compare with the specifications. According to the preliminary results obtained, a reflection on an optimization of the thermal model of the machine will be made.

Fig. 12 illustrates the simplified thermal model circuit used to study the machine. The thermal capacities have been neglected since only the steady-state operation of the machine is considered. Q_rotor, Q_ws, Q_st, Q_sy describe the iron losses of the rotor, the cooper losses, the iron losses of the stator, and the iron losses of the stator yoke, respectively. The individual thermal resistances are identified in Table III. Tambiant is assigned as boundary conditions, it is fixed at 38°C (a temperature slightly higher than the natural temperature of blood in the human body) to evaluate the heating in the real cases.

The following reasonable assumptions are made to reduce the solution scale and improve the calculation efficiency:

- When the motor operates under steady-state conditions, the losses are uniformly distributed within each heat source.
- Heat transfer is only in the axial and radial directions.
- The equivalent thermal conductivity of the winding can be obtained by semi-analytical homogenizations or by averaging using numerical tools. The approach used refers to [11,12].
- The equivalent thermal conductivity is $0.7488\ \mathrm{W/(m.°C)}$.
- Heat transfer coefficient in natural convection (laminar regime) is $10\ \mathrm{W/(m^2.°C)}$.
- The model does not have a cooling casing. The goal is to reduce the size and weight of the system, so a system cooled by natural convection is preferred. Forced convection cooling systems are ruled out.

TABLE III
THERMAL RESISTANCES

Name	Description
R_{rotor}	Thermal resistance of rotor core
R_{mag}	Thermal resistance of the magnet pole
R_{ag}	Convection thermal resistance of air gap
R_{teeth}	Thermal resistance of stator teeth
R_{sloth}	Thermal resistance of the coil
R_{yoke}	Thermal resistance of conduction in the stator yoke.

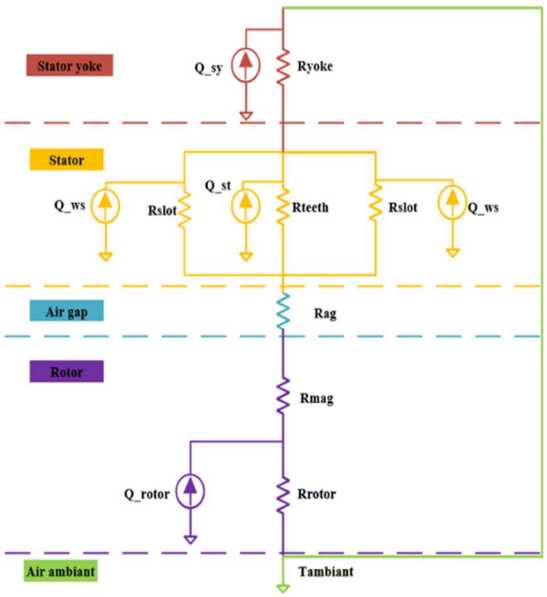

Fig. 12. The equivalent circuit to the simplified thermal model of the motor in steady state.

Fig. 13 shows the temperature distribution of the machine. The simulation showed that the temperature on the slots does not exceed 58°C, and the external temperature of the stator does not exceed 38°C. This value is lower than the critical operating temperature of the pump, which corresponds to the blood denaturation temperature. (42°C). The maximum temperature rise in the prototype is 65°C at the slots, an acceptable level given the lack of cooling of the machine.

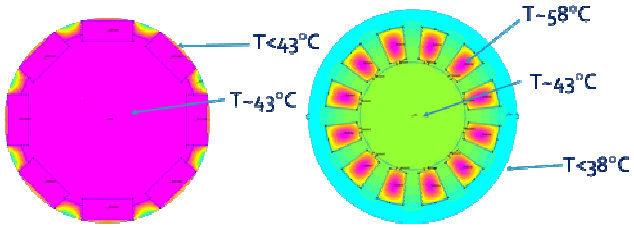

Fig. 13. Temperatures map with FEMM.

To verify the correctness of the calculation results of FEM and the Lumped Parameter Thermal Network (LPTN), it is necessary to test the temperature rise. Two thermocouple resistors are buried in the stator slot of the prototype (shown in section IV) to test the temperature rise of the winding. The comparison of test results is shown in Table IV.

TABLE IV
RESULTS COMPARISON

Maximum average temperature (°C)	LTPN	FEM	Test result
Wingding (slots)	60	58	65

The thermal model developed was not used in optimization because the preliminary results are entirely satisfactory in temperature and heating. However, a more in-depth thermal study will be carried out later.

IV. PMSM PROTOTYPE

The prototype of the PMSM has been manufactured to test performance. Manufacturing stages and pictures of the prototype motor are illustrated in Fig. 14. The pictures show the active part of the motor: the stator and the rotor, magnet assembly, the stator with concentrated windings, and finalized motor structure. Also, electro-erosion cutting method is used to form the laminations stator. NdFeB magnets are glued on the surface of the rotor, the choice of magnets fell on standard products on shelves. The main difficulties encountered are the geometric imperfections of the magnets, which required rectification, and the mechanical alignment of the various elements on the test bench. In addition, an experimental test bench shown in Fig. 15 is used to get the performance results of the motor. The experimental system is composed of the designed prototype motor, a load motor with extremely low cogging torque levels (1%), a torque sensor, and an angular position sensor. A field-oriented control implemented on a dSPACE MicroLabBox controller board is used to drive the motor. The specifications of this testing motor are reported in Table V.

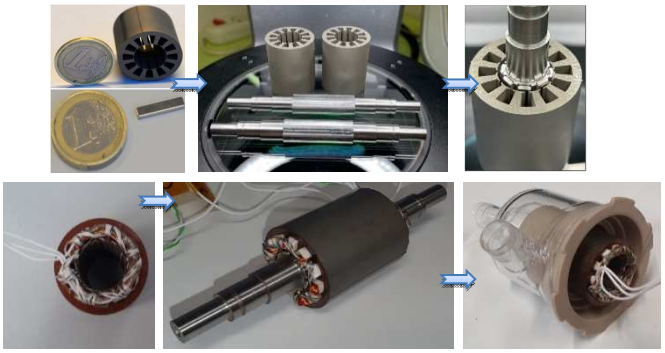

Fig. 14. Manufacturing stages of the PMSM prototype.

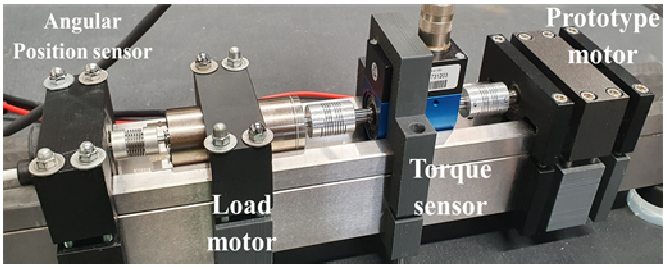

Fig. 15. Motor test bench.

TABLE V
IMPORTANT SPECIFICATION OF THE TESTING MOTOR

Specifications: Symbols	Values (Units)
Back emf constant: K_e	0.017 $(Vrms/rad.s)$
Torque constant: K_t	0.020 $(Nm/Arms)$
Maximum bus voltage: U_{DC}	12 (V)
Stator per phase resistance: R_S	3.32 (Ω)
Stator per phase inductance: L_S	0.40 (mH)
Q-axis inductance: L_q	0.36 (mH)
D-axis inductance: L_q	0.38 (mH)
Inertia: J	$7.5916e^{-6}$ $(kg.m^2)$
Mechanical constant of test bench:τ	150 (ms)
Motor mass: m	100 (g)

No-load tests of the PMSM prototype are carried out. The cogging torque comparison between FEA and experimental results is given in Fig. 16. The figure shows that the values obtained from experimental results are slightly higher than FEA. Due to minor imperfections in rotor manufacturing and assembly, some cogging and vibrations are noticed during tests. The waveforms are different because the torque meter used averages the measurement.

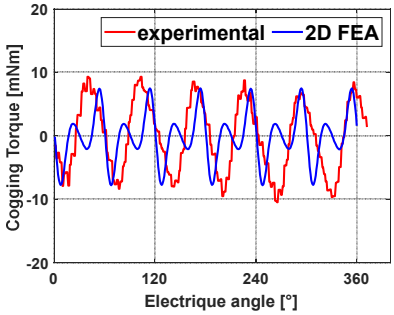

Fig. 16. Cogging torque waveforms.

Phase-Phase back-EMF voltage waveforms at 820 rpm are illustrated in Fig. 17. Also, the waveform of the test results matches well with the FEA results, as shown in the figure. It should be mentioned that the shape of the back EMF is slightly different between experimental analysis and FEA analysis. Due to the grinding of the magnets, during the assembly of the machine, a geometric adjustment of the shape of the magnets was necessary (at the corners). This correction generated an error between the experimental results and the FEA analysis of the order of 5% at the level of the no-load tests. The error was verified by an EF analysis of the machine with deformed magnets. There is a slight deformation of the top of the waveforms due to the geometric error between the model and the prototype.

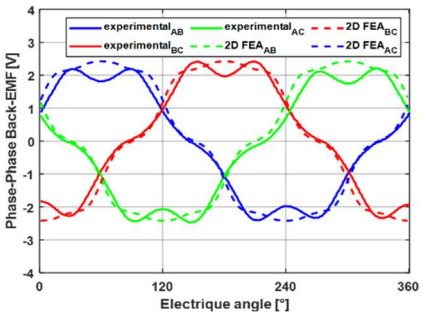

Fig. 17. Phase back-EMF comparison between 2D/3D FEA and experimental results (@820rpm).

In addition, the machine is rotated at different no-load speed values and phase-to-phase counter-EMFs are obtained. Fig. 18 shows the comparison between the FEA and the experimental results of the peak values of the phase-phase counter-EMF at different rotor speeds. The figure shows that the FEA results correspond well to the experimental data with minor errors. For example, the maximum back-EMF voltage at 555 rpm is 1.4 V for FEA and 1.3 V for experimental data.

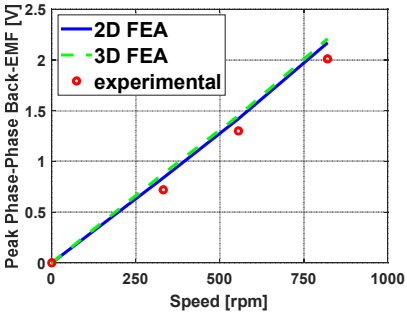

Fig. 18. Peak values of phase-phase back-EMF vs. speed comparison between 2D/3D FEA and experimental results.

The average torque at different currents obtained from both FEA and experimental is illustrated in Fig. 19. The average torque is obtained by injecting the sinusoidal experimental currents corresponding to each operation point in the FE analysis. The results show that the experimental torque is slightly larger than the FEA model for points greater than 400 mA. As also seen from the figure, the results match well with a 4% error.

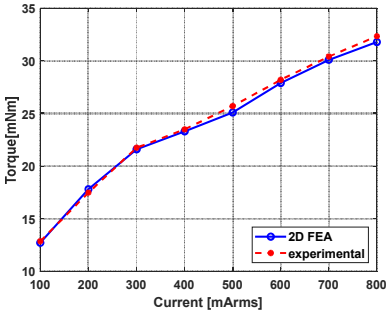

Fig. 19. Torque-current comparison between FEA and experimental.

V. Conclusion

This paper proposes the design of a PMSM to develop of a portable artificial lung. Its pre-dimensioning is carried out using the design of experiments method. The detailed 2D and 3D finite element analyses are completed, and the performance results of the motor are summarized using both 2D and 3D FEA simulations. Machine torque and efficiency variations are also simulated. A slight difference between 2D and 3D FEA is observed at both no-load and on-load analyses. A prototype machine has been built to validate the analysis. The results obtained from FEA are compared to experimental measurement. For EMF and torque average, very good agreements are obtained. The comparison results show that the design approach works well. The developed motor is distinguished by its weight of 100 g compared to several kilos for current motors. Concerning the hydraulic performances of the pump, they are being evaluated; a flow rate of 3 L/min is obtained for a speed of 4500 rpm.

Future works will concern the improvement of the cogging torque. Noise and vibration will be also evaluated. The temperature of the pump associated with the actuator will be evaluated. A second more innovative actuator is under development, and its validation will be the subject of future works and publications.

VI. REFERENCE

[1] R. Vazquez and D.F. Larson., "Plasma protein denaturation with graded heat exposure, " Perfusion, 2013.

[2] F. Gilon and P. Brochet., "Shape Optimization of a Permanent Magnet Motor using the Experimental Design Method, " IEEE Trans. Magn, vol. 35, no, 3, May 1999.

[3] J. Goupy, Les plans d'Expériences, Revue Modulad, no. 34, pp. 74–116, 2006.

[4] S. Vivier, F. Gilon, and P. Brochet, "Optimization Techniques Derived from Experimental Design Method and Their Application to the Design of a Brushless Direct Current Motor, " IEEE Trans. Magn., vol. 37, no. 5, Sep 2001.

[5] N. Bianchi, L. Alberti, M. Popescu, and T. J. E. Miller, "MMF Harmonics Effect on the Embedded FE Analytical Computation of PM Motors," IEEE Trans. Ind. Appl., vol. 46, no. 2, pp. 812–820, Mar. 2010.

[6] F. Bu, Z. Yang, Y. Gao, Z. Pan, T. Pu, M. Degano, and C. Gerada, "Speed Ripple Reduction of Direct-Drive PMSM Servo System at Low-Speed Operation Using Virtual Cogging Torque Control Method, " IEEE Trans. Ind. Elec., vol. 68, no. 1, Jan 2021.

[7] A. Boglietti, A. Cavagnino, M. Lazzari, and M. Pastorelli, "Predicting Iron Losses in Soft Magnetic Materials With Arbitrary Voltage Supply: An Engineering Approach, " IEEE Trans. Magn., vol. 39, no. 2, 2003.

[8] X. Ding, M. Bhattacharya and C.Mi, "Simplified Thermal Model of PM Motors Hybride Vehicle Applications Taking into Account Eddy Current Loss in Magnets," Journal of Asian Electric Vehicles, Volume 8, Number1, June 2010.

[9] P.H. Mellor, D. Roberts and D.R. Tuner, "Lumped parameter thermal model for electrical machines of TEFC design, " IEEE Proceedings-B, Vol. 138, No.5 5, September 1991.

[10] R. Wrobel and R.H. Mellor, "A General Cuboidal Element for Three-Dimensional Thermal Modelling, " IEEE Trans. Magn, vol. 46, no. 8, August 2010.

[11] L. Idoughi, X. Mininger, F. Bouillault, L. Bernard and E. Hoang, " Thermal Model With Winding Homogenization and FIT Discretization for Stator Slot, " IEEE Trans. Magn, vol. 47, no. 12, December 2011.

[12] G.W. Milton, "Bounds on the transport and optical properties of a two-component composite material, " J. Appl. Phys., vol. 52, pp. 5294-5304,1981.

VII. BIOGRAPHIES

A. Sahnoune received his master's in electrical engineering in 2019 from Paris-Saclay University, France. He is now a Ph.D. student at CentraleSupelec. His current research interests include design, finite element analysis and optimization of electric machines and drives.

M. Hage-Hassan received her B.S. degree in mechanical engineering from the faculty of engineering, Lebanon, Masters in Product Design and Development from Ecole Centrale de Nantes in 2010 and a Ph.D. degree in electrical engineering from University Paris-Saclay in 2014. She is now an Associate Professor at CentraleSupelec. Her current research interests include design and optimization of electric machines and drives.

C. Marchand graduated from the Ecole Normale Supérieure de Cachan, France. He received the Ph.D. and the HDR degrees from the Université Paris-Sud, Paris, France in 1991 and 1999 respectively. He joined the Université Paris-Sud as an Assistant Professor in 1994 and became a Full Professor in 2000. Since 1988, he has been a researcher at the Laboratoire de Génie Electrique de Paris (LGEP) where his research interests are in eddy current nondestructive testing and in the design and control of electrical actuators. Since 2015, he is head of the Group of Electrical Engineering of Paris (GeePs laboratory)

J. Guihaire received his M.D. degree in general surgery in 2012 from Rennes University Medical School, France, and his Ph.D. degree and Habilitation for Direction of Research respectively in 2014 and 2021, both from Paris-Saclay University, France. As attending cardiac surgeon, he is the head of the advanced heart failure program and leads the preclinical research program of ex vivo heart perfusion at Marie Lannelongue Hospital, Paris-Saclay University, France.

O. Mercier received his MD degree in general surgery in 2006 from Paris-Saclay University and graduated the French Board of Thoracic and Cardiovascular Surgery in 2009. He has been appointed as full Professor of Thoracic Surgery at Paris-Saclay University since 2014 and leads the bioengineering innovation program of Marie Lannelongue Hospital, Paris-Saclay University, France.

G. Krebs received his Ph.D. degree and Habilitation for Direction of Research respectively in 2006 and 2017, both from Paris-Saclay University, France. He is now an Associate Professor at Paris-Saclay University since 2008. His current research interests include design, optimization and finite element analysis of electric machines and drives.